



Since January 2020 Elsevier has created a COVID-19 resource centre with free information in English and Mandarin on the novel coronavirus COVID-19. The COVID-19 resource centre is hosted on Elsevier Connect, the company's public news and information website.

Elsevier hereby grants permission to make all its COVID-19-related research that is available on the COVID-19 resource centre - including this research content - immediately available in PubMed Central and other publicly funded repositories, such as the WHO COVID database with rights for unrestricted research re-use and analyses in any form or by any means with acknowledgement of the original source. These permissions are granted for free by Elsevier for as long as the COVID-19 resource centre remains active.



Artificial intelligence-assisted colorimetric lateral flow immunoassay for sensitive and quantitative detection of COVID-19 neutralizing antibody

Haoyang Tong^{a,b,1}, Chaoyu Cao^{a,b,1}, Minli You^{a,b,**}, Shuang Han^{b,c}, Zhe Liu^{a,b,d}, Ying Xiao^e, Wanghong He^{b,f}, Chang Liu^{a,b}, Ping Peng^{b,g}, Zhenrui Xue^{b,g}, Yan Gong^h, Chunyan Yao^{b,g}, Feng Xu^{a,b,*}

^a The Key Laboratory of Biomedical Information Engineering of Ministry of Education, School of Life Science and Technology, Xi'an Jiaotong University, Xi'an, 710049, PR China

^b Bioinspired Engineering and Biomechanics Center (BEBC), Xi'an Jiaotong University, Xi'an, 710049, PR China

^c Department of Gastroenterology of Honghui Hospital, Xi'an, 710054, PR China

^d Department of Rehabilitation Medicine, The First Affiliated Hospital of Xi'an Jiaotong University, Xi'an, 710061, PR China

^e Clinical Laboratory, Xi'an Jiaotong University School Hospital, Xi'an, 710061, PR China

^f Key Laboratory of Shaanxi Province for Craniofacial Precision Medicine Research, College of Stomatology, Xi'an Jiaotong University, Xi'an, 710049, PR China

^g Department of Transfusion Medicine, Southwest Hospital, Third Military Medical University (Army Medical University), Chongqing, 400038, PR China

^h Diyinan Biotech Company, Suzhou, 215000, PR China

ARTICLE INFO

Keywords:

COVID-19

Neutralizing antibody

Lateral flow immunoassay

Artificial intelligence

Polydopamine

ABSTRACT

Currently, vaccination is the most effective medical measure to improve group immunity and prevent the rapid spread of COVID-19. Since the individual difference of vaccine effectiveness is inevitable, it is necessary to evaluate the vaccine effectiveness of every vaccinated person to ensure the appearance of herd immunity. Here, we developed an artificial intelligent (AI)-assisted colorimetric polydopamine nanoparticle (PDA)-based lateral flow immunoassay (LFIA) platform for the sensitive and accurate quantification of neutralizing antibodies produced from vaccinations. The platform integrates PDA-based LFIA and a smartphone-based reader to test the neutralizing antibodies in serum, where an AI algorithm is also developed to accurately and quantitatively analyze the results. The developed platform achieved a quantitative detection with 160 ng/mL of detection limit and 625–10000 ng/mL of detection range. Moreover, it also successfully detected totally 50 clinical serum samples, revealing a great consistency with the commercial ELISA kit. Comparing with commercial gold nanoparticle-based LFIA, our PDA-based LFIA platform showed more accurate quantification ability for the clinical serum. Therefore, we envision that the AI-assisted PDA-based LFIA platform with sensitive and accurate quantification ability is of great significance for large-scale evaluation of vaccine effectiveness and other point-of-care immunoassays.

In 2019, the sudden outbreak of coronavirus disease 2019 (COVID-19) spreads rapidly around the world, causing serious harm to the human health and global economy (Zhu et al., 2020). According to data released by the World Health Organization (WHO) by September 2021, the cumulative number of confirmed cases has exceeded 200 million, the death toll has exceeded 4 million, and the number of infections is increasing by millions every week (<https://covid19.who.int>). Currently,

vaccination is the most effective medical intervention to impede the development of epidemics and help us to return to normal life (Nel and Miller, 2021). Through constant efforts of vaccine development scientists and enterprise, five major vaccines have been available for the public (Zhao et al., 2020). However, the effectiveness of existing vaccines is still a concern and the corresponding individual difference is inevitable (Ibarrondo et al., 2021; Lv et al., 2020). Therefore, it is

* Corresponding author. The Key Laboratory of Biomedical Information Engineering of Ministry of Education, School of Life Science and Technology, Xi'an Jiaotong University, Xi'an, 710049, PR China.

** Corresponding author. The Key Laboratory of Biomedical Information Engineering of Ministry of Education, School of Life Science and Technology, Xi'an Jiaotong University, Xi'an, 710049, PR China.

E-mail addresses: yuminli@xjtu.edu.cn (M. You), fengxu@mail.xjtu.edu.cn (F. Xu).

¹ These authors contributed equally to this work.

necessary to evaluate the vaccine effectiveness for every vaccinated person to ensure the herd immunity (Heaton, 2021).

Considering the large number of vaccinated people, the ideal evaluation method for vaccine effectiveness should be cheap, fast and easy-to-operate. For now, the popular method to evaluate the vaccine effectiveness is to test the neutralizing antibodies, since neutralizing antibody is the key molecule to inhibit the binding of virus to host cells (Earle et al., 2021). At present, there are several neutralization test (NT) methods. For instance, the plaque reduction neutralization test (PRNT) is one kind of traditional method of neutralizing antibodies test. However, due to its low throughput and long duration, PRNT is not practical for large-scale serodiagnosis and vaccine evaluation (Murua et al., 2020). To address this, a fluorescent-based high-throughput assay was developed to detect COVID-19 neutralizing antibodies that yields equivalent results to the traditional PRNT assays (Murua et al., 2020). Furthermore, a chemiluminescence reduced neutralization test (CRNT)-based antibody detection system was also developed to measure the neutralizing antibodies to SARS-CoV-2 under BSL2 conditions (Tani et al., 2021). However, NT methods not only require severe experimental conditions and professional persons, but also need a long process of cell culture. ELISA is the most commonly used antibody detection method with high sensitivity and specificity, which could be completed within several hours. For example, a neutralizing antibody detection method was developed that does not require any live virus or cells and can be completed in 1–2 h on an ELISA plate with 95–100% sensitivity (Tan et al., 2020). Additionally, the S1 structural domain of the spike protein is also used to detect IgG antibodies against COVID-19 in an indirect ELISA for the detection of immune responses in vaccinated people over 1 h (Krahling et al., 2021). Although the ELISA method is high throughput, it still needs hours to output the results and severely depends on large equipment and skilled operators. Moreover, its high cost also hinders the applications for large scale evaluation of vaccine effectiveness (Berg et al., 2015).

Recently, lateral flow immunoassay (LFIA) has attracted wide attention, due to its advantages of simple operation, rapid detection, low cost, enabling on-site testing without aid of large equipment (Mohammad Lukman et al., 2018). Therefore, the LFIA is superior to ELISA for large-scale evaluation of vaccine effectiveness in aspects of detection cost (11–16 dollars for LFIA vs. ~50–65 dollars for ELISA), detection time (<20 min for LFIA vs. 1–2 h for ELISA) and operation process (one step for LFIA vs. 8 steps for ELISA) (Mohit et al., 2021). For instance, a gold nanoparticle (AuNP)-based LFIA was developed for monitoring early immune responses to COVID-19 and for large-scale screening to assess SARS-CoV-2 vaccine efficacy (Roda et al., 2021). Another Surface-Enhanced Raman Scattering (SERS) based-LFIA was also developed to achieve accurate and rapid screening of COVID-19 and to provide an effective complementary means (Liu et al., 2021a). At present, commercial AuNP-based LFIA has been widely used due to its simple operation and visual readout of results. However, the AuNP-based LFIA is limited by low sensitivity, disable quantification (Shirshahi et al., 2020) and potential threat to environment (Du et al., 2020), which may lead to misjudgments for vaccine effectiveness. Therefore, the development of a highly sensitive, environment-friendly, and quantitative LFIA platform for accurate neutralizing antibody detection is necessary for epidemic prevention and control.

Here, we developed a colorimetric LFIA platform to accurately and quantitatively detect the neutralizing antibodies against COVID-19, by integrating a polydopamine (PDA) nanoparticles (NPs)-based LFIA and an associated artificial intelligent (AI) analysis algorithm. To conveniently read out and analyze the detection results, we assembled a portable smartphone-based reader using Lego blocks to image the LFIA results and output it for the AI algorithm to accurately analyze the neutralizing antibody concentration. By comparing with commercial AuNP-based LFIA, the developed colorimetric LFIA platform exhibited a higher sensitivity. Moreover, the developed colorimetric LFIA was able to quantify the neutralizing antibody concentration in serum samples

and exhibit great consistence with the ELISA results. Thus, we envision that the developed colorimetric LFIA platform is a powerful tool for the low-cost, fast and large-scale vaccine effectiveness evaluation.

1. Results and discussion

Principle of PDA-based LFIA Platform. Currently, it is urgently needed to rapidly and accurately detect neutralizing antibodies against COVID-19 for the evaluation of convalescent plasma therapy and vaccine effectiveness. To address this, we developed an AI-assisted PDA-based LFIA platform composed of a PDA-based LFIA (Fig. 1a) and a smartphone-based reader (Fig. 1b and c). The PDA-based LFIA contains a test line and a control line, with test line immobilized with ACE2 antigens and control line immobilized with goat anti-mouse IgG. The PDA probe is conjugated with receptor binding domain (RBD) of viral spike protein (S protein) and mouse IgG. When the negative sample is added to the LFIA, the PDA probe is combined with the test line and control line on the NC membrane (upper Fig. 1a). If the positive sample (containing neutralizing antibodies) is added, the neutralizing antibodies will first bind specifically with the PDA probe to form PDA-NA complex. Under the capillary force, the PDA-NA complex will flow through the test line and control line. Since the RBD on PDA probe surface has bound with neutralizing antibodies, the PDA-NA complex is not able to be captured by ACE2 on the test line, while the PDA probes without binding neutralizing antibodies will be captured on test line. After that, the excessive PDA probes would bind to the goat anti-mouse IgG on the control line (bottom Fig. 1a). By measuring the colorimetric signal of test and control lines, the concentrations of neutralizing antibodies can be calculated.

To accurately and conveniently read out the results, we assembled a smartphone-based portable reader by using Lego blocks (Fig. 1b), which can shield external light permeation and remian a stable light environment under illumination of the smartphone flash. At the bottom of portable reader, a slot is designed for PDA-based LFIA. To read the test and control lines of PDA-based LFIA, a dark passageway is left and covered with a black cotton. The black cotton can avoid the reflection of the flash light. At the top of reader, there is a support plate to put the smartphone and a readout window for the smartphone camera (Fig. 1c). With the smartphone flash, a bright and clear image of PDA-based LFIA can be captured by the smartphone. After the analysis of trained AI algorithm, the obtained images are converted to quantitative results of neutralizing antibodies (Fig. 1d).

Characterization of PDA NPs. The PDA NPs are selected here as the probes of LFIA, due to its pronounced absorption for visible wavelengths (Meredith and Sarna, 2006). Moreover, the PDA NPs are biodegradable (Molnár, 2020), making the PDF-based LFIA disposable and environment-friendly. However, the strong adhesion of PDA NPs makes them easily attached on the NC membrane (Lee et al., 2007). Therefore, if we directly modified the antibodies on the PDA NPs surface, the obtained PDA probes would be mostly non-specific absorbed on test line resulting in a false negative result (Fig. 2a). To address this issue, we first coated the PDA NPs with three polyelectrolyte layers (*i.e.*, PSS, PAH, PVP) by layer-by-layer assembly technology (Pastoriza-Santos et al., 2006). Then, a dense silica layer was formed to prevent non-specific adsorption of PDA NPs. Next, COOH-PEG-Silane was modified on the surface of PDA NPs to further enhance the anti-fouling ability of PDA NPs and provide carboxyl groups to following antibodies modification. The obtained PDA probes could efficiently decrease the non-specific absorption on test line in positive group (Fig. 2b). The solutions of naked PDA, PDA@Polymer³@SiO₂, and PDA@polymer³@SiO₂@-PEG-RBD are stable and uniformly dispersed in water (Fig. 2c). We observed an obvious increase of particle size as reflected by the TEM images of PDA NPs before and after surface modification (Fig. 2d), indicating the successful fabrication of core-shell structure. Meanwhile, the zeta potential and dynamic light scattering (DLS) were also tested during coating process (Fig. S1 and Fig. 2e and f). The zeta potential

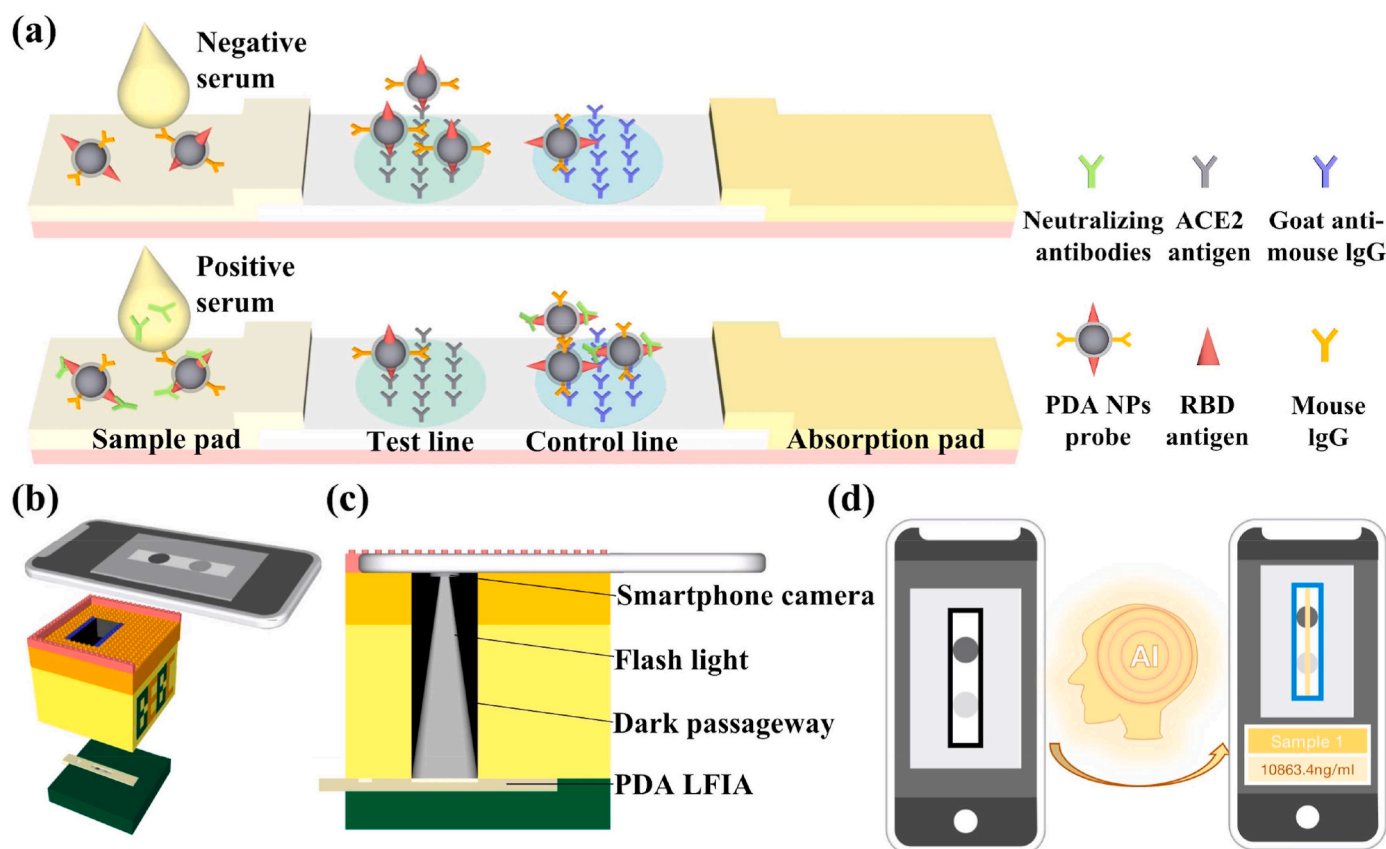


Fig. 1. Schematic illustration of PDA-based LFIA platform. (a) The PDA-based LFIA work principle. (b) The smartphone-based portable reader assembled by Lego blocks. (c) The internal structure of smartphone-based portable reader. (d) The AI algorithm used for the analysis of PDA-based LFIA images.

results showed that both the polyelectrolyte layer and SiO₂ layer decrease the negative potential of naked PDA NPs, while the RBD coating increases the negative potential. The DLS results confirmed the continuous size increase of PDA NPs after sequential surface coating. The final DLS size of PDA@polymer³@SiO₂@PEG-RBD is ~270 nm. Both DLS and zeta potential results confirmed the successful surface modifications of PDA NPs. Moreover, we compared the UV-vis spectra of PDA NPs and AuNPs at the same mass fractions (4.5%) (Fig. 2g). The results showed that the PDA NPs possess higher absorption during visible wavelengths than AuNPs, indicating that the PDA NPs could contribute higher colorimetric signal than AuNPs when used in LFIA. Notably, the eyes readable colorimetric signal is the overall absorption in the visible range (400–700 nm). Therefore, the LSPR peak shift of AuNPs with different sizes has few effect on the colorimetric signal.

Optimization of PDA-based LFIA. We modified the PDA NP with RBD and mIgG together, where the RBD aims to detect neutralizing antibodies and mIgG aims to react with C line to verify the validation of this test. To optimize the sensitivity of PDA-based LFIA, we adjusted two major factors that are related to the detection sensitivity, *i.e.*, the proportions of RBD and mouse IgG modified on PDA NPs surface and the added PDA probes volume per LFIA. The former affects the binding efficiency of PDA probes to target neutralizing antibodies or ACE2 on test line, while the latter affects the total signal intensity and the decrease rate of signal intensity caused by the same concentration of target. Firstly, three kinds of concentration ratio (*i.e.*, 1:2, 1:1 and 2:1) of RBD and mouse IgG were conjugated with PDA NPs (Fig. 3a). 10 μL PDA probe was used to test a same positive sample. By comparing the densities of test line and control line in positive group and negative group, we observed obvious decrease for the test line density and increase for the control line density at the groups of 1:1 and 2:1 ratio of RBD and mouse IgG (Fig. 3a). Here, the optical density values of test line (T) and

control line (C) were measured by image J and the ratio of T/(T + C) was used to reflect the target concentration. By calculating the T/(T + C), the quantification results revealed the group with 1:1 RBD and mouse IgG ratio exhibited an extremely significant difference (Fig. 3b). Therefore, the 1:1 ratio of RBD and mouse IgG was selected as the optimized ratio to modify the PDA probes and use in the next experiments. To optimize the added PDA probe volume per test, 12.5 μL, 10 μL and 7.5 μL PDA probes were added to test positive sample and negative sample, respectively (Fig. 3c). There is no difference for the group with 12.5 μL PDA probes, and significant difference for the groups with 10 μL and 7.5 μL PDA probes (Fig. 3d). Lastly, we chose 10 μL as the optimized PDA probe volume, since more PDA probes could enable a wider detection range. Here, we compared the detection performance of the PDA-based LFIA with wet method and dry method. The results revealed no obvious difference between these two methods (Fig. S2). Thus, we used PDA-based LFIA with wet method to conduct the following experiments. Additionally, to verify the PDA-based LFIA enabling higher colorimetric signal than AuNP-based LFIA, the two kinds of LFIA with same mass fraction of probes were used to test a same serum (Fig. S3). The results revealed that the PDA-based LFIA showed nearly 4 folds colorimetric signal than AuNP-based LFIA, where the positive and negative groups of PDA-based LFIA showed extremely significant differences ($p < 0.001$), while the AuNP-based LFIA showed significant differences ($p = 0.011$).

Smartphone-based AI analysis algorithm. To accurately quantify the results of the PDA-based LFIA, we designed a smartphone-based AI algorithm to analyze the LFIA pictures and output the neutralizing antibody concentrations. To avoid the interfering of shooting environment and simplify the capture of LFIA results, a portable reader was assembled using Lego blocks (Fig. 4a). The previous study in our group has developed a smartphone APP to quantify the LFIA results by measuring density value. However, the quantification process needs to manually

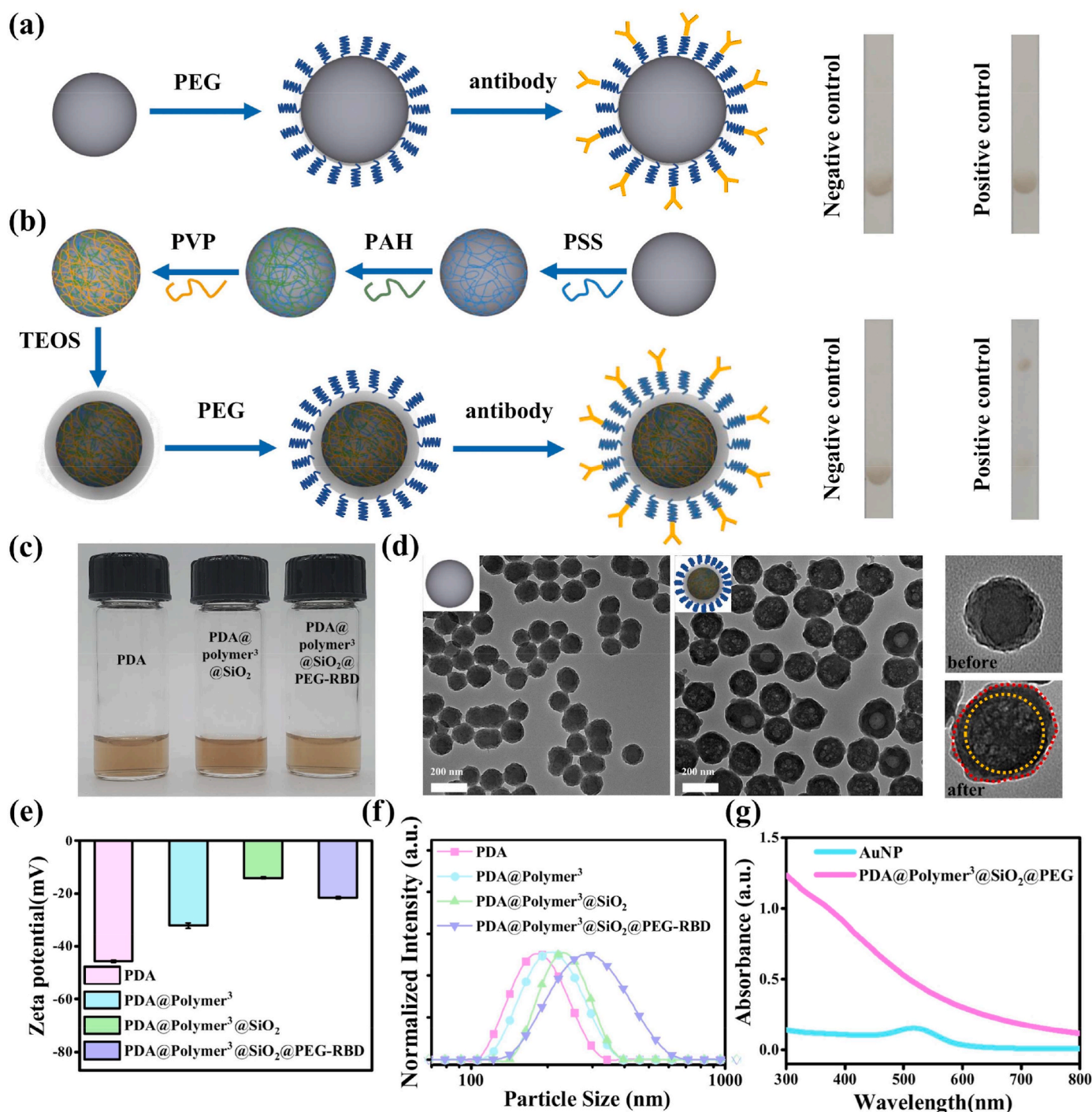


Fig. 2. Characterization of PDA NPs. (a) Modification process of PDA@PEG@Ab NPs (left) and comparison of the results of negative control and positive control (right). (b) Modification process of PDA@Polymer³@SiO₂@PEG@Ab NPs (left) and comparison of the results of negative control and positive control (right). (c) Homogeneous dispersion of PDA, PDA@Polymer³@SiO₂, PDA@polymer³@SiO₂@PEG-RBD solutions. (d) TEM images of PDA before and after surface modifications. The (e) zeta potential and (f) DLS characterization for PDA NPs during surface modification process. (g) UV-Vis spectra of PDA NPs and AuNPs at the mass fraction of 4.5‰.

select the detection region, where the subjective judgment may cause biased results. To address this issue, we utilized an AI algorithm to accurately identify the detection region, analyze the density distribution of detection region and output the quantification concentrations. Specifically, it is necessary to detect the position of strips from images shot by the smartphone reader at first. We applied the vision transformer (ViT) (Dosovitskiy et al., 2020) to our system to detect the position stably and accurately. ViT is a deep learning method recently developed

for computer vision tasks, which applies attention mechanism to image processing and reaches a benchmark performance in many tasks, like classification (Chen et al., 2021), instance segmentation (Balaji et al., 2020), etc. We detected the position of strips by three steps. The first is preprocessing. Since the light source is controllable and fixed, we removed the black background from the original images with threshold segmentation and derived a cropped smaller image, which only contains the commercial cover and the strip. Then to keep all images in the same

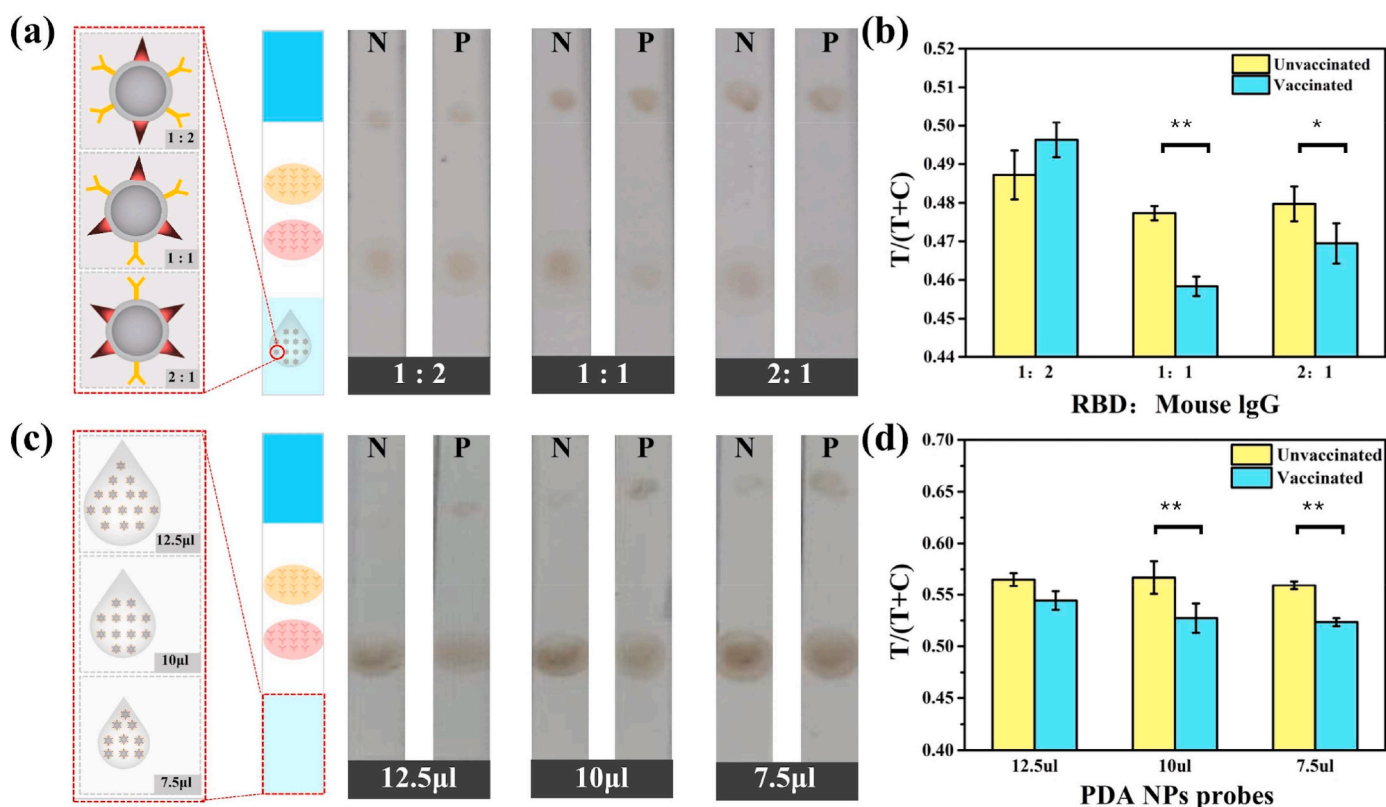


Fig. 3. Optimization of the factors related to PDA-based LFIA sensitivity. (a) The schematic illustration and experimental results of the optimization of RBD and mouse IgG ratio modified on PDA NPs surface. The optimized ratios are 1:2, 1:1 and 2:1 from left to right, respectively. (b) The quantitative results of the RBD and mouse IgG ratio optimization. (c) The schematic illustration and experimental results of the optimization of the added PDA probes volume. The optimized volumes are 12.5 μL , 10 μL and 7.5 μL from left to right, respectively. (d) The quantitative results of the added PDA probes volume optimization. $p < 0.05$ indicates significant difference (*), and $p < 0.01$ indicates extremely significant difference (**).

size, which is necessary for inputting them into our neural network, we resized all images into 512×512 . The next step is inputting the resized images to the backbone convolutional neural network (CNN). We used ResNet50 (He et al., 2016) as our backbone CNN and replaced batch normalization (Ioffe and Szegedy, 2015) layers with group normalization (Wu and He, 2018) layers to reduce errors from small batch size (8 in our task). The outputs of the backbone CNN are feature maps in size of $32 \times 32 \times C$, where C is the channel number of the feature maps. The backbone CNN was trained from scratch. The last step is predicting position with ViT. We cropped the feature maps to 16×16 patches, each of which has a size of $1 \times (4 \times C)$. These patches with a trainable box vector was concatenated to form a matrix of shape $257 \times (4 \times C)$ and embedded by different weights, then declared as query, key and value for further self-attention calculation. The last part of the network is a multilayer perceptron (MLP) head that will output the strip's bounding box, represented by coordinate of the strip's vertexes in the image. The loss curve of the AI algorithm was shown in Fig. S4. After the prediction of the ViT, we plotted a horizon center line of the predicted bounding box on the strip. Fig. 4b shows some examples of our detection results, chosen from training set and test set. The RGB values among the center lines are transformed to gray intensities and then plotted as intensity distribution curves (Fig. 4c). For positive LFIA samples, there should be two peaks in each curve. We found the two peak values, corresponding to the test line and the control line, and noted them as T and C, respectively. The value of $T/(T + C)$ will be calculated for further quantitative analysis. Most images in both training set and test set are detected with high intersection over unions (IoUs) (Fig. 4d). IoU is a metric to measure consistency between predicted bounding box and ground truth box, calculated by the ratio of overlap area and the area encompassed by the two boxes. For further practicality, we developed a

smartphone application with our trained network to analyze our PDA-based LFIA, see Fig. S5. The IoUs distribution for different type of phones was shown in Fig. S6 and Fig. 4d. This represents our bounding box detection results can be recognized as largely coincident with ground truths and can be used for further analysis.

To further prove the stability of our model to predict images from different type of phones, we did the cross validation based on phone types. There are totally three folds for cross validation: fold 1, training set = Huawei and iPhone, test set = Samsung; fold 2, training set = Huawei and Samsung, test set = iPhone; fold 3, training set = iPhone and Samsung, test set = Huawei. Our model can reach a robust high performance on each fold (Fig. S7), which indicates that our model is stable when apply to different types of phones. However, the performance of the AI trained with three kinds of phone images still surpasses those of fold 1–3. We also conducted an ablation experiment of box vector, which proves that it is necessary of box vector to guarantee a high IoU in our model (Fig. S8). Since the dataset had a small size, we also compared our model with other common traditional computation vision algorithms to prove the necessity of applying deep learning model. Scale-invariant feature transform (SIFT) (Lowe, 1999) and Oriented FAST and rotated BRIEF (ORB) (Rublee et al., 2011) were compared with our method. They performed poorly for the PDA-LFIA task (Table S3 and Fig. S9) and needed different thresholds when applied to different images. Thus, these methods require users to understand relevant algorithm knowledge and manually adjust parameters, which is contrary to the concept of POCT.

Verification of clinical samples. To verify the developed PDA-based LFIA platform for the clinical serum samples, we collected 30 clinical sera to test the developed PDA-based LFIA platform and compared the results with those of commercial ELISA kits (Fig. 5a). First, gradient

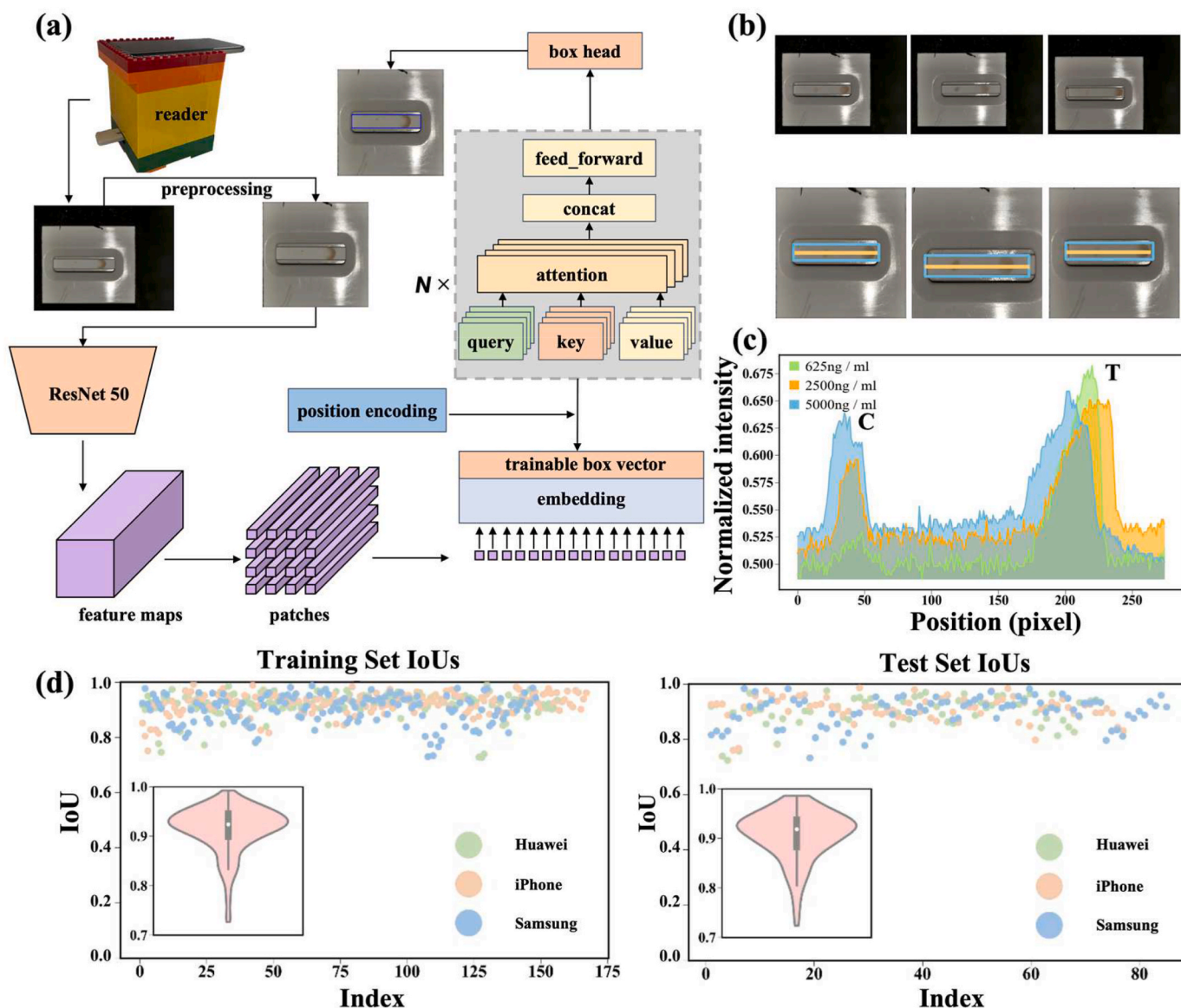


Fig. 4. Deep learning algorithm and strip position detection results. (a) Workflow of the algorithm. For the input image, the dark background will be removed and the remain part will be resized to a square image for further detection. Feature maps will be derived from the resized image by ResNet 50. Then the feature maps are cropped to patches and embedded to feed the transformer encoding layers, which are marked with a gray box. In order to get the position of the strip, we applied a box head, which is an MLP, to the attention vector. (b) Some examples of results detected by our algorithm. Upper three: results examples from PDA strip dataset. Lower three: results examples with horizontal center line of the bounding box (the yellow lines). (c) Examples of gray intensities distribution curves. The two peaks in the curve are noted as C and T. (d) Training set IoUs (left) and test set IoUs (right) predicted from the trained model. The violin plot was plotted on bottom left for each subfigure to show the distribution of IoUs.

concentrations were spiked to obtain the standard curves of the PDA-based LFIA platform and commercial ELISA kit (Supplemental Figs. S10 and 11). The standard curve reveals the detection limit of PDA-based LFIA is 160 ng/mL (Fig. S11a). And the corresponding linear dynamic range and slope are 625–10000 ng/mL and -0.06 , respectively (Fig. S11b). The results show that PDA LFIA is able to specifically distinguish between negative and positive samples (Fig. S12). Notably, some reported LFIAs with signal amplification strategies exhibit higher sensitivity than the developed PDA-based LFIA here (Huang et al., 2016; Liu et al., 2021b; Soh et al., 2020). However, these LFIAs with signal amplification are normally accompanied with high cost, complex operation and complicated fabrication process, which are not suitable to the evaluation of vaccination effectiveness. Moreover, based on the judgment standard (*i.e.*, cut-off = $1/2$ OD_{blank}) of the commercial SARS-CoV-2 neutralizing antibody ELISA kit, 1713 ng/mL is calculated as the cutoff value to distinguish negative and positive samples. Thus,

the detection limit with ng/mL level has satisfied the demand of neutralizing antibody detection to distinguish the people with effective vaccination or not. After that, 30 clinical sera (containing 3 non-vaccinated people and 27 vaccinated people) were used to test the neutralizing antibody concentrations by ELISA kit and PDA-based LFIA platform (Fig. 5b and c). The whole test time of PDA-based LFIA platform for each sample is around 20 min, while the ELISA kit needs 2 h for each test. Based on the cutoff value provided by the ELISA kit, 17 of 27 vaccinators showed positive neutralizing antibody, while 10 showed negative results. The possible reason is that corresponding volunteers have been vaccinated for several months, and their antibody concentrations have decreased to a very low level over time or their immunoreactions have not been activated yet (Dan et al., 2020). Therefore, the evaluation of vaccine effectiveness should dynamically monitor the neutralizing antibody of vaccinated people within the several weeks after vaccination. The PDA-based LFIA platform revealed the similar

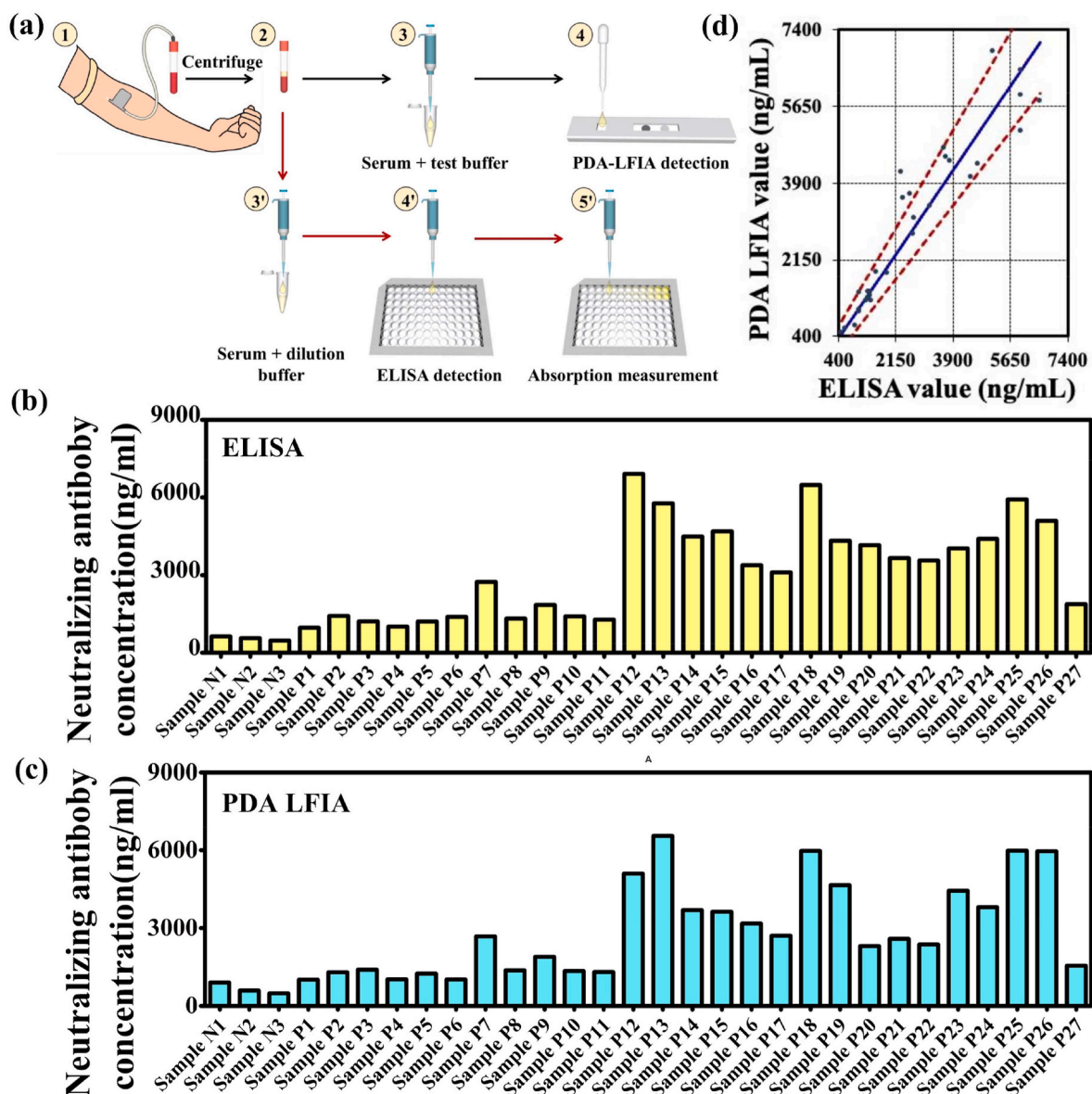


Fig. 5. Quantitative detection of neutralizing antibody concentrations in clinical samples. (a) Schematic illustration of the detection process of 30 serum samples (containing 3 non-vaccinated people and 27 vaccinated people) by commercial ELISA kit and the PDA-based LFIA platform. The quantitative detection results of (b) commercial ELISA kit and (c) PDA-based LFIA platform for the 30 serum samples (containing 3 non-vaccinated people and 27 vaccinated people). (d) Passing-Bablok regression plots of the neutralizing antibody detection results obtained from the ELISA kit and the PDA-based LFIA platform. Solid blue line represents the linear regression plot, and two red dotted lines represent the 95% CI range. The regression equation for neutralizing antibody detection was obtained $y = 1.09$ (95% CI, 0.96 – 1.27) $x - 88.18$ (95% CI, -358.81 to -141.50).

results with that of ELISA kit, where 16 show positive results and 11 show negative results. To verify the linear correlation between PDA-based LFIA platform and ELISA kit, the Passing-Boblok regression and Spearman's rank correlation were used. The obtained regression equations and Spearman's coefficient were $y = 1.09$ (95% CI, 0.96 – 1.27) $x - 88.18$ (95% CI, -358.81 to -141.50) and 0.951 ($P < 0.001$), respectively (Fig. 5d). The slope of Passing-Boblok regression equation is ranged between 0.8 – 1.2 , and Spearman's coefficient is close to 1 and $P < 0.001$, proving that there exists a good linear correlation between the two methods for neutralizing antibody detection.

Dynamic monitoring of neutralizing antibodies after COVID-19 vaccination. Since the vaccine effectiveness shows obvious individual difference (Brosh-Nissimov et al., 2021; Chung et al., 2020), it is necessary to dynamically monitor the neutralizing antibodies of every vaccinated person in early period of vaccination (Fig. 6a). To verify the role of AI-assisted PDA-based LFIA in dynamic monitoring the

neutralizing antibodies of vaccinated people, we tracked the neutralizing antibody levels changes in serum at different timelines in four COVID-19 vaccinated volunteers (Fig. 6b). Neutralizing antibody levels in the sera of 4 vaccinated subjects were detected successively at different timelines, i.e., before inoculation, 30 days after the first inoculation, and 20–95 days after the second inoculation. The four volunteers all showed minimal increase for the neutralizing antibodies after the first inoculation. After the second inoculation, the neutralizing antibodies in volunteer 1 and 2 showed a rapid increase within three weeks and then slowly decrease after that, where the peaks both reached at 21 days and are 10,954 ng/mL and 27,013 ng/mL, respectively. The neutralizing antibody level of volunteer 4 showed a similar trend with volunteer 1 and 2. While, its peak at 35 days after the second inoculation. The level of neutralizing antibody in volunteer 3 was significantly lower than that in other volunteers, even if there was an increase trend observed, which reveals that volunteer 3 may be not responsive to this

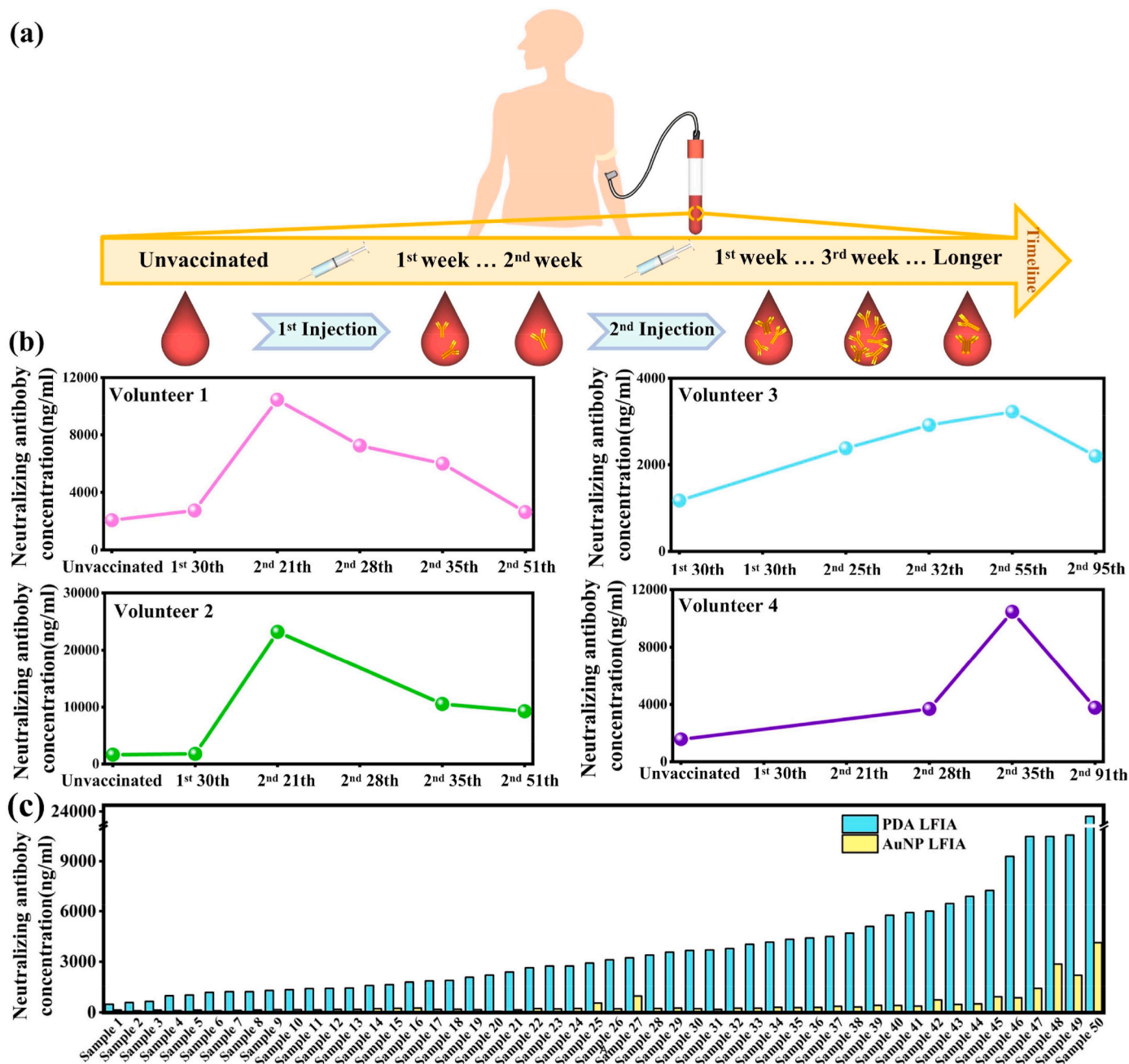


Fig. 6. Dynamic monitoring of the neutralizing antibody concentrations of four vaccinated volunteers by AI-assisted PDA-based LFIA. (a) Timeline schematic of the dynamic monitoring of the neutralizing antibodies. (b) Dynamic monitoring of AI-assisted PDA-based LFIA platform for the neutralizing antibody concentrations of four volunteers. (c) Comparison of quantitative results of PDA-based LFIA and commercial AuNP-based LFIA assays for 50 serum samples.

kind of vaccination. Above results confirmed two conclusions proposed by previous studies about vaccination effectiveness (Bar-On et al., 2021; Feng et al., 2021; Flaxman et al., 2021; Pritchard et al., 2021; Wesemann, 2022). The first is that the second reinforcing inoculation is necessary for simulate the immune system to produce neutralizing antibodies with high concentration. The second is that individual differences are inevitably in population, which supports that the dynamic monitoring of neutralizing antibodies is necessary. Based on dynamic monitoring results, vaccinated person could decide if accept the reinforcing inoculation and the inoculation time. To compare the detection performance of AI-assisted PDA-based LFIA and commercial AuNP-based LFIA for neutralizing antibodies, we quantified the neutralizing antibody levels of 50 serum samples (20 samples from the four dynamic monitoring volunteers at different time, 3 samples from

non-vaccinated people and 27 samples from vaccinated people shown in Fig. 5) based on the standard curves (Figs. S11 and S13). The results showed that all the quantified results of AuNP-based LFIA is very low, compared with the AI-assisted PDA-based LFIA platform. Especially for the samples with low neutralizing antibody level, it is quite difficult for AuNP-based LFIA to distinguish them (Fig. 6c and Fig. S14). Therefore, the developed AI-assisted PDA-based LFIA platform provides a better quantification ability for the clinical serum samples than the commercial AuNP-based LFIA.

2. Conclusion

In summary, we have developed an AI-assisted PDA-based LFIA platform that integrates a PDA-based LFIA, a smartphone-based reader

and an AI analysis algorithm to achieve portably automated and accurate quantification for colorimetric LFIA. Three innovation points are promoted in this study. Firstly, the strong absorption in visible region and low cost of PDA NPs improve the sensitivity and reduce the cost of PDA-based LFIA compared to the AuNPs-based LFIA. Moreover, the silica coated core-shell PDA nanoparticles also avoids the non-specific absorption of naked PDA nanoparticles. Secondly, the integration of the AI algorithm and portable reader enables automated and accurate quantification for colorimetric LFIA. At last, the developed PDA-based LFIA platform successfully achieved the evaluation of vaccine effectiveness with simple operation, short detection time and low cost. Therefore, we envision that the developed PDA-based LFIA platform could be a timely manner for the large-scale evaluation of vaccine effectiveness.

3. Materials and methods

Materials. Dopamine hydrochloride, tetraethyl orthosilicate (TEOS), N-(3-Dimethylaminopropyl)-N'-ethylcarbodiimide hydrochloride (EDC), dimethyl sulfoxide (DMSO), bovine serum albumin (BSA), triton X-100, tween 20, trizma base were purchased from Sigma-Aldrich. Sodium polystyrene sulfonate standard (PSS, Mw = 14900) was obtained from Shanghai ZZBIO CO., LTD. Poly (allylamine hydrochloride) (PAH, Mw = 15000), polyvinylpyrrolidone (PVP, Mw = 10000) were purchased from Shanghai Macklin Biochemical Co., Ltd. COOH-PEG-Silane was purchased from Chongqing Yusi Medicine Technology Co., Ltd. Ammonia solution (25%) was obtained from Tianjin Beilian Chemical Reagen Co., Ltd. Sucrose was obtained from Tianjin Hedongqu Chemical Reagen Co., Ltd. Sodium chloride (NaCl) was obtained from Tianjin Tianli Chemical Reagent Co., Ltd. Ethanol, methanol, isopropyl alcohol were purchased from Tianjin Fuyu Chemical Reagen Co., Ltd. Sulfo-NHS was obtained from Shanghai Medpep Co., Ltd. 2-(N-morpholino)ethanesulfonic acid (MES), 2-[4-(2-hydroxyethyl) piperazin-1-yl] ethanesulfonic acid (HEPES) were obtained from MP Biomedicals, LLC. Glycine was purchased from Sangon Biotech (Shanghai) Co., Ltd. All reagents were of analytical grade and used without any purification. Lateral flow test strips were made by Suzhou Diyinan Biological Technology Co., Ltd. SARS-CoV-2 ACE2 antigen, SARS-CoV-2 RBD antigen, Mouse IgG, Goat anti-mouse IgG were purchased from Beijing Baisaisi Biotechnology Co., Ltd. The serum samples of SARS-CoV-2 vaccinated volunteers from Xi'an Red Cross Hospital and the First Affiliated Hospital of Xi'an Jiaotong University. The participants have signed a written informed consent to conduct scientific research. SARS-CoV-2 Neutralizing Antibody ELISA Kit was purchased from Wuhan Huamei Biological Engineering Co., Ltd. The AuNP-based LFIA was obtained from Hangzhou Frenovo Biotech Co., Ltd.

Synthesis of PDA NPs. The PDA NPs were synthesized following the previous protocol (Liu et al., 2013). 10 mL ethanol, 0.75 mL ammonia solution were added to 22.5 mL deionized water in a round bottom flask, and stirring in 30 °C water bath for 30 min. Then quickly added dopamine hydrochloride solution (0.659 mmol dopamine hydrochloride dissolves in 2.5 mL deionized water) into the solution and stirred for 24 h. The solution was mixed with acetone at a ratio of 1:2 and precipitated for 24 h. The precipitate was collected by centrifugation (8000 rpm, 10 min, 25 °C) and the supernatant was removed. The precipitate was washed 3 times with acetone and then redispersed in deionized water and stored at 4 °C.

Polyelectrolyte-Mediated Silica Coated of PDA NPs. The silica coating of PDA NPs were synthesized following the previous protocol (Pastoriza-Santos et al., 2006). Add 5 mL of PDA NPs dropwise to 5 mL of 2 g/L PSS aqueous solution containing 6 mM NaCl with vigorous stirring for 3 h. Centrifuge (8000 rpm, 10 min, 25 °C) the solution twice to remove excess electrolytes and resuspend in 5 mL of deionized water. Then PSS-coated PDA was added dropwise to 5 mL of 2 g/L PAH aqueous solution containing 6 mM NaCl with vigorous stirring for 3 h. Centrifuge (8000 rpm, 10 min, 25 °C) the solution twice and resuspend in 5 mL of

deionized water. Next, 5 mL of PAH-coated PDA was mixed with 5 mL of 4 g/L PVP and stirred overnight. Centrifuge (8000 rpm, 10 min, 25 °C) PVP-coated PDA and resuspend the precipitate in 0.2 mL deionized water. After adding 1 mL of isopropanol, the solution was added to 0.46 mL of water under vigorous stirring, followed by 1.43 mL of ammonia-isopropanol solution (3.84 vol%). Then 0.4 mL TEOS-isopropanol (0.97 vol%) was added under gentle stirring and reacted for 2 h. PDA@SiO₂ was centrifuged (8000 rpm, 10 min, 25 °C) three times and redispersed in methanol.

Surface Modification of PDA NPs. After dissolving COOH-PEG-silane in methanol (50 μL, 10 mM), 950 μL PDA@SiO₂ was added and stirred vigorously for 2 h. Centrifuge (8000 rpm, 10 min, 25 °C) with methanol and deionized water twice each. PDA@PEG was resuspended in deionized water.

Conjugation of Antibodies to PDA NPs. 200 μL PDA@PEG solution was washed for three times with 200 μL DMSO-MES buffer (33% v/v DMSO, 20 mM MES) and resuspend in 150 μL DMSO-MES buffer, sonicate until photodispersion is homogeneous. 6 μL of 6 mg/mL EDC, 6 μL of 6 mg/mL NHS were added into PDA DMSO-MES solution at room temperature and activated under sonication for 30 min, the activated product was washed with DMSO-MES buffer and redispersed in 200 μL DMSO-MES buffer. 800 μL of 20 mM MES buffer and 37.5 μL of different concentration ratios of SARS-CoV-2 RBD antigen and mouse IgG solution (1:1, 1:2, 2:1, i.e., 0.5 μg/mL: 0.5 μg/mL, 0.33 μg/mL: 0.67 μg/mL, 0.67 μg/mL: 0.33 μg/mL) were added to the solution and incubated for 2 h at 37 °C with shaking at 100 r/min. 30 μL Glycine stop buffer was added, the obtained PDA-antigen complex was washed with storage buffer (50 mM glycine, 0.1% NaN₃, 0.03% v/v triton) and redispersed in storage buffer and stored at 4 °C.

Calculation of the mass fraction of AuNPs and PDA NPs. An empty 2 mL tube was used to measure its mass (m_1). 1.5 mL (m) NPs solution was first centrifuged at 12000 rpm for 30 min at room temperature. The precipitate was dried in an oven at 60 °C for 2 days. Then, the mass of the tube containing dried precipitate (m_2). The mass fraction can be calculated by the following equation: mass fraction = $(m_2 - m_1) / (m - m_1)$.

Characterization of PDA NPs. The morphology of PDA NPs was characterized by transmission electron microscopy (TEM) using an FEI Talos F200C instrument at an accelerating voltage of 200 kV. Zeta potentials and dynamic light scatter (DLS) of PDA NPs were determined using a Zetasizer Nano ZSE. The UV-Vis-NIR spectra of the PDA NPs were obtained with a UV-Vis-NIR spectrophotometer (PE Lambda950). The optical density was measured using a multifunctional microplate detector (Tecan Spark 10M) under 450 nm excitation light. Images of PDA-based LFIA and AuNP-based LFIA were obtained by smartphone (HUAWEI P30 Pro). All the measurements were performed at room temperature.

Fabrication of PDA-based LFIA. The LFIA were fabricated following our previous protocol (You et al., 2017). The glass fiber pad, nitrocellulose membrane and absorbent pad were mounted sequentially on the support pad using plastic adhesive with an overlap of 2 mm between two adjacent pads. Then, the assembled pads were cut by Matrix™ 2360 Programmable Sheer (Kinematic Automation, Sonora, CA, USA) to a width of 2.5 mm strips. The detection and control zones were immobilized with 0.5 μL of 1 mg/mL SARS-CoV-2 ACE2 antigen and 0.5 μL of 0.2 mg/mL goat anti-mouse IgG, respectively. The resulting test strips were dried at 37 °C for 2 h and then stored at 25 °C for further use.

Clinical serum samples. We collected sera from 12 non-vaccinated volunteers and 27 vaccinated volunteers. All the volunteers are healthy people without major chronic diseases and have never been infected by any type of SARS virus. Their basic information including gender, age, collection date, and 1st/2nd injection dates are listed in Table S2.

Assays with ELISA kit. Neutralizing antibody was sequentially diluted to different multiples with sample diluent (0, 9.75, 19.5, 39, 78, 159, 312, 625, 1250, 2500, 5000, 10000 ng/mL), and 50 μL neutralizing antibody or diluted Sample was added to each well of a 96-well plate.

Mix well with the pipette or shake the plate gently for 60 s. Cover with plate sticker and incubate at 37 °C for 1 h. Wash the plate 5 times. Soak for 2 min each time, 250 µL/well, and shake dry. Add 90 µL substrate solution to each well in turn and develop at 37 °C for 20 min under protection from light. Add 50 µL termination solution to each well in turn to terminate the reaction. Within 5 min after the termination of the reaction, the optical density (OD) of each well was measured sequentially at 450 nm using the enzyme standard. Calculate the binding rate (%) : the OD value of Standard and sample are divided by the OD value of blank group and multiplied by 100%.

$$\text{Binding rate (\%)} = \frac{B}{B_0} \times 100\%$$

B —the average absorbance value of the sample or Standard
 B₀ —the average absorbance value of the 0 ng/ml (0 nM) Standard

Assays with Lateral Flow Test Strips. Standard neutralizing antibody solutions (0, 78, 159, 312, 625, 1250, 2500, 5000, 10000, 20000, 40000 ng/mL) were prepared by stepwise dilution. Wet method: 30 µL standard neutralizing antibody solution or volunteer serum was mixed with 10 µL PDA probe solution and 60 µL HSLF buffer (270 mM NaCl, 100 mM HEPES buffer, 0.5% w/v tween 20, 1% w/v BSA). The obtained solution was added to the test strips for testing. Dry method: 100 µL the PDA probe solution was centrifuged (8000 rpm, 10 min, 25 °C) and resuspended in B9 buffer (8.5 g/L tris, 10 g/L BSA, 50 g/L alginate, 200 g/L sucrose) to 50 µL and then 5 µL was dropped onto the binding pad. The obtained test strips were dried in a electric thermostaticdrying oven at 37 °C for 2 h. Next, 60 µL HSLF buffer and 30 µL standard neutralizing antibody solution or volunteer serum were mixed and added to the test strips for testing. AuNP-based LFIA : 30 µL volunteer serum was mixed with 10 µL AuNP probe solution and 60 µL HSLF buffer. The obtained solution was added to the test strips for testing. Commercial AuNP-based LFIA : 30 µL standard neutralizing antibody solution or volunteer serum was mixed with 60 µL buffer. The obtained solution was added to the test strips for testing. After 20 min, the results of LFIA were read out with a Nikon D90 camera or smartphone. The optical density values of test line (T) and control line (C) were measured by image J and the ratio of T/(T + C) was used to reflect the target concentration.

Smartphone reader. The reader was built with classic bricks of Lego, where a cavity dark room inside the reader was aligned with the test area of the test strips, the top of the device was designed to carry a recess for smartphones, and the light source for taking pictures was provided by the flash of the phone. To avoid the interference of reflected light from colorful Lego blocks, we pasted a black fluffy cloth on the inside surface of the reader. All the structure sizes of the Lego blocks are 7.8 mm * 7.5 mm * 9.5 mm, and the sizes of the whole Lego reader is 90 mm * 90 mm * 110 mm.

3.1. Construct of AI algorithm

Dataset: We created our dataset from standard concentration gradient samples. To make our AI algorithm more general and stable, we used three types of mobile phone, Huawei, iPhone and Samsung, to take photos for PDA-based LFIAs. For each standard concentration gradient sample, we used different types of mobile phones to take photos when the strip was in different positions. For each type of mobile phones, we totally took 114, 120 and 115 images, respectively. Then these images were flipped for data augmentation. Among all images, 234 images are randomly chosen as training set, and the other 115 images consisted the test set.

Network settings. In our task, we used group normalization instead of batch normalization to support our small batch size; for each group normalization layer, the group number was set to 8. The channel number of the output of the ResNet50 was set to 1024, and the patch size was set to 2 × 2. Here, 256 patches were generated for the feature map. Then

these patches are embedded to a dimension of 1024 and concatenated with a randomly initialized trainable vector to input to the encoder. The encoder is consisted of 6 alternating layers, each of which has an 8-head self-attention module. A linear layer whose input size is 1024 was then used to predict the position of the test strip. The position of a strip was represented by a bounding box that can fully enclose the strip, described by $[x_1, y_1, x_2, y_2]$. (x_1, y_1) and (x_2, y_2) are the coordinates of the box's upper-left vertex and the lower-right vertex respectively.

Training. For the training step, we defined our loss function as the combination of Distance IoU (Zheng et al., 2020) and MSE loss as follow:

$$\text{Loss} = 1 - \text{IoU} + \frac{\rho^2(\hat{\mathbf{b}}, \mathbf{b})}{c^2} + \text{MSE}(\hat{\mathbf{b}}, \mathbf{b})$$

Here, $\rho()$ is the function to calculate Euclidean distance, c means the diagonal length of the smallest enclosing box for the two boxes. IoU is the intersection over union of predicted bounding box $\hat{\mathbf{b}} = (\hat{x}_1, \hat{y}_1, \hat{x}_2, \hat{y}_2)$ and the ground truth bounding box $\mathbf{b} = (x_1, y_1, x_2, y_2)$, can be calculated by:

$$\text{IoU} = \frac{|\hat{\mathbf{b}} \cap \mathbf{b}|}{|\hat{\mathbf{b}} \cup \mathbf{b}|}$$

MSE is the mean square error,

$$\text{MSE}(\hat{\mathbf{b}}, \mathbf{b}) = \frac{1}{4} \sum (\hat{b}_i - b_i)^2$$

The network was trained on 1.4 GHz Quad-Core Intel Core i5 for 50 epochs with a batch size of 8. The initial learning rate was set as 5×10^{-6} , and optimized by the AdamW optimizer (Loshchilov and Hutter, 2017) with a weight decay rate of 1×10^{-4} . The network showed a great sensitivity to the learning rate; thus, we reduce the learning rate to a half every 10 epochs to reach a stable training performance. To inhibit overfitting, we add random Gaussian noise to all images on each training epoch. The trained network was then used to detect all samples in training set and test set.

Other traditional computer vision algorithms. We compared SIFT and ORB to prove the necessity of applying AI algorithm in our task. SIFT and ORB can both detect features in two images and compare those features based on Euclidean distance to check if these two images have the same object. For each type of phone, we prepared a reference image and extract its features and use matcher (FLANN based matcher for SIFT and BFMatcher for ORB) to match these features in others images. Low distance matches are then used to locate strips in images.

Calculation of neutralizing antibody concentration. A horizontal line is draw cross the middle of the output images by the network, resulting a gray intensity distribution curve. Values from two peaks represent T and C values, respectively. The ratio of T/(T + C) was used to reflect the target concentration.

Code availability

Codes for our project are available at <https://github.com/XJTU-BEBC/PDA-LFIA.git>.

CRedit authorship contribution statement

Haoyang Tong: Conceptualization, Methodology, Validation, Formal analysis, Investigation, Writing – original draft, Writing – review & editing. **Chaoyu Cao:** Conceptualization, Methodology, Validation, Formal analysis, Investigation, Writing – original draft, Writing – review & editing. **Minli You:** Conceptualization, Writing – review & editing, Supervision, Project administration. **Shuang Han:** Investigation, Formal analysis, Resources. **Zhe Liu:** Investigation, Formal analysis, Resources. **Ying Xiao:** Methodology, Resources. **Wanghong He:** Methodology, Resources. **Chang Liu:** Investigation, Methodology. **Ping Peng:** Investigation, Formal analysis. **Zhenrui Xue:** Investigation, Methodology.

Yan Gong: Investigation, Methodology. **Chunyan Yao:** Methodology, Resources. **Feng Xu:** Writing – review & editing, Supervision, Project administration.

Declaration of competing interest

The authors declare that they have no known competing financial interests or personal relationships that could have appeared to influence the work reported in this paper.

Acknowledgments

We thank Miss Huimin Tong and Miss Hang Guo at Instrument Analysis Center of Xi'an Jiaotong University for their assistance with TEM and DSL analysis. This work was supported by the National Key Research and Development Program of China (2018YFC1707702), the National Natural Science Foundation of China (22104119), the Fundamental Research Funds for the Central Universities of China (xzy012019067), the General Financial Grant from the China Postdoctoral Science Foundation (2019M663741), the Key Program for Science and Technology Innovative Research Team in Shaanxi Province of China (2017KCT-22), the Natural Science Foundation of Shaanxi Province of China (2021JQ-013).

Appendix A. Supplementary data

Supplementary data to this article can be found online at <https://doi.org/10.1016/j.bios.2022.114449>.

References

- Balaji, E., Brindha, D., Balakrishnan, R., 2020. Supervised machine learning based gait classification system for early detection and stage classification of Parkinson's disease. *Appl. Soft Comput.* 94, 106494.
- Bar-On, Y.M., Goldberg, Y., Mandel, M., Bodenheimer, O., Freedman, L., Kalkstein, N., Mizrahi, B., Alroy-Preis, S., Ash, N., Milo, R., Huppert, A., 2021. Protection of BNT162b2 vaccine booster against Covid-19 in Israel. *N. Engl. J. Med.* 385 (15), 1393–1400.
- Berg, B., Cortazar, B., Tseng, D., Ozkan, H., Feng, S., Wei, Q., Chan, R.Y.-L., Burbano, J., Farooqui, Q., Lewinski, M., Di Carlo, D., Garner, O.B., Ozcan, A., 2015. Cellphone-based hand-held microplate reader for point-of-care testing of enzyme-linked immunosorbent assays. *ACS Nano* 9 (8), 7857–7866.
- Brosh-Nissimov, T., Orenbuch-Harroch, E., Chowes, M., Elbaz, M., Neshet, L., Stein, M., Maor, Y., Cohen, R., Hussein, K., Weinberger, M., Zimhony, O., Chazan, B., Najjar, R., Zayyad, H., Rahav, G., Wiener-Well, Y., 2021. BNT162b2 vaccine breakthrough: clinical characteristics of 152 fully vaccinated hospitalized COVID-19 patients in Israel. *Clin. Microbiol. Infect.*
- Chen, H., Li, C., Li, X., Wang, G., Hu, W., Li, Y., Liu, W., Sun, C., Yao, Y., Teng, Y., 2021. GasHis-Transformer: A Multi-Scale Visual Transformer Approach for Gastric Histopathology Image Classification arXiv preprint arXiv:2104.14528.
- Chung, Y.H., Beiss, V., Fiering, S.N., Steinmetz, N.F., 2020. COVID-19 vaccine frontrunners and their nanotechnology design. *ACS Nano* 14 (10), 12522–12537.
- Dan, J.M., Mateus, J., Kato, Y., Hastie, K.M., Yu, E.D., Faliti, C.E., Grifoni, A., Ramirez, S. I., Haupt, S., Frazier, A., Nakao, C., Rayaprolu, V., Rawlings, S.A., Peters, B., Krammer, F., Simon, V., Saphire, E.O., Smith, D.M., Weiskopf, D., Sette, A., Crotty, S., 2020. Immunological memory to SARS-CoV-2 assessed for up to eight months after infection. *bioRxiv*: the preprint server for biology.
- Dosovitskiy, A., Beyer, L., Kolesnikov, A., Weissenborn, D., Zhai, X., Unterthiner, T., Dehghani, M., Minderer, M., Heigold, G., Gelly, S., 2020. An Image Is Worth 16x16 Words: Transformers for Image Recognition at Scale arXiv preprint arXiv:2010.11929.
- Du, J., Wu, S., Hu, Z., Yu, Z., Zhao, D., Bai, Y., 2020. Green synthesis of salt-tolerant gold nanoparticles for the rapid qualitative detection of *Listeria monocytogenes* in lateral flow immunoassay. *J. Mater. Sci.* 55 (32), 15426–15438.
- Earle, K.A., Ambrosino, D.M., Fiore-Gartland, A., Goldblatt, D., Gilbert, P.B., Siber, G.R., Dull, P., Plotkin, S.A., 2021. Evidence for antibody as a protective correlate for COVID-19 vaccines. *Vaccine* 39 (32), 4423–4428.
- Feng, S., Phillips, D.J., White, T., Sayal, H., Aley, P.K., Bibi, S., Dold, C., Fuskova, M., Gilbert, S.C., Hirsch, I., Humphries, H.E., Jepson, B., Kelly, E.J., Plested, E., Shoemaker, K., Thomas, K.M., Vekemans, J., Villafana, T.L., Lambe, T., Pollard, A.J., Voysey, M., Adlou, S., Allen, L., Angus, B., Anslow, R., Asselin, M.-C., Baker, N., Baker, P., Barlow, T., Beveridge, A., Bewley, K.R., Brown, P., Brunt, E., Buttigieg, K. R., Camara, S., Charlton, S., Chiplin, E., Cicconi, P., Clutterbuck, E.A., Collins, A.M., Coombes, N.S., Clemens, S.A.C., Davison, M., Demissie, T., Dinesh, T., Douglas, A.D., Duncan, C.J.A., Emary, K.R.W., Ewer, K.J., Felle, S., Ferreira, D.M., Finn, A., Folegatti, P.M., Fothergill, R., Fraser, S., Garland, H., Gatcombe, L., Godwin, K.J., Goodman, A.L., Green, C.A., Hallis, B., Hart, T.C., Heath, P.T., Hill, H., Hill, A.V.S., Jenkin, D., Kasanyinga, M., Kerridge, S., Knight, C., Leung, S., Libri, V., Lillie, P.J., Marinou, S., McGlashan, J., McGregor, A.C., McInroy, L., Minassian, A.M., Mujajidi, Y.F., Penn, E.J., Petropoulos, C.J., Pollock, K.M., Proud, P.C., Provstgaard-Morys, S., Rajapaska, D., Ramasamy, M.N., Sanders, K., Shaik, I., Singh, N., Smith, A., Snape, M.D., Song, R., Shrestha, S., Sutherland, R.K., Thomson, E.C., Turner, D.P.J., Webb-Bridges, A., Wrin, T., Williams, C.J., 2021. Correlates of protection against symptomatic and asymptomatic SARS-CoV-2 infection. *Nat. Med.* 27 (11), 2032–2040.
- Flaxman, A., Marchevsky, N.G., Jenkin, D., Aboagye, J., Aley, P.K., Angus, B., Belij-Rammerstorfer, S., Bibi, S., Bittaye, M., Cappuccini, F., Cicconi, P., Clutterbuck, E.A., Davies, S., Dejnirattisai, W., Dold, C., Ewer, K.J., Folegatti, P.M., Fowler, J., Hill, A. V.S., Kerridge, S., Minassian, A.M., Mongkolsapaya, J., Mujajidi, Y.F., Plested, E., Ramasamy, M.N., Robinson, H., Sanders, H., Sheehan, E., Smith, H., Snape, M.D., Song, R., Woods, D., Srean, G., Gilbert, S.C., Voysey, M., Pollard, A.J., Lambe, T., Adlou, S., Aley, R., Ali, A., Anslow, R., Baker, M., Baker, P., Barrett, J.R., Bates, L., Beadon, K., Beckley, R., Bell, J., Bellamy, D., Beveridge, A., Bissett, C., Blackwell, L., Bletchly, H., Boyd, A., Bridges-Webb, A., Brown, C., Byard, N., Camara, S., Cifuentes Gutierrez, L., Collins, A.M., Cooper, R., Crocker, W.E.M., Darton, T.C., Davies, H., Davies, J., Demissie, T., Di Maso, C., Dinesh, T., Donnellan, F.R., Douglas, A.D., Drake-Brockman, R., Duncan, C.J.A., Elias, S.C., Emary, K.R.W., Ghulam Farooq, M., Faust, S.N., Felle, S., Ferreira, D., Ferreira Da Silva, C., Finn, A., Ford, K.J., Francis, E., Furze, J., Fuskova, M., Galiza, E., Gibertoni Cruz, A., Godfrey, L., Goodman, A.L., Green, C., Green, C.A., Greenwood, N., Harrison, D., Hart, T.C., Hawkins, S., Heath, P.T., Hill, H., Hillson, K., Horsington, B., Hou, M.M., Howe, E., Howell, N., Joe, C., Jones, E., Kasanyinga, M., Keen, J., Kelly, S., Kerr, D., Khan, L., Khozoe, B., Kinch, J., Kinch, P., Koleva, S., Kwok, J., Larkworthy, C.W., Lawrie, A. M., Lazarus, R., Lees, E.A., Li, G., Libri, V., Lillie, P.J., Linder, A., Long, F., Lopez Ramon, R., Mabbett, R., Makinson, R., Marinou, S., Marlow, E., Marshall, J.L., Mazur, O., McEwan, J., McGregor, A.C., Mokaya, J., Morey, E., Morshead, G., Morter, R., Muller, J., Mweu, P., Noristani, R., Owino, N., Polo Peralta Alvarez, M., Platt, A., Pollock, K.M., Poulton, I., Provstgaard-Morys, S., Pulido-Gomez, D., Rajan, M., Ramos Lopez, F., Ritchie, A., Roberts, H., Rollier, C., Rudiansyah, I., Sanders, K., Saunders, J.E., Seddiqi, S., Sharpe, H.R., Shaw, R., Silva-Reyes, L., Singh, N., Smith, D.J., Smith, C.C., Smith, A., Spencer, A.J., Stuart, A.S.V., Sutherland, R., Szigeti, A., Tang, K., Thomas, M., Thomas, T.M., Thompson, A., Thomson, E.C., Török, E.M., Toshner, M., Tran, N., Trivett, R., Turnbull, I., Turner, C., Turner, D.P.J., Ulaszewska, M., Vichos, I., Walker, L., Watson, M.E., Whelan, C., White, R., Williams, S.J., Williams, C.J.A., Wright, D., Yao, A., 2021. Reactogenicity and immunogenicity after a late second dose or a third dose of ChAdOx1 nCoV-19 in the UK: a substudy of two randomised controlled trials (COV001 and COV002). *Lancet* 398 (10304), 981–990.
- He, K., Zhang, X., Ren, S., Sun, J., 2016. Deep residual learning for image recognition. *Proc. IEEE Conf. Comput. Vis. Pattern Recognit.* 770–778.
- Heaton, P.M., 2021. Herd immunity: the journey is as important as the destination. *J. Infect. Dis.* 224 (6), 931–933. WHO Coronavirus (COVID-19) Dashboard. <http://covid19.who.int>.
- Huang, X.L., Aguilar, Z.P., Xu, H.Y., Lai, W.H., Xiong, Y.H., 2016. Membrane-based lateral flow immunochromatographic strip with nanoparticles as reporters for detection: a review. *Biosens. Bioelectron.* 75, 166–180.
- Ibarrondo, F.J., Hofmann, C., Fulcher, J.A., Goodman-Meza, D., Mu, W., Hausner, M.A., Ali, A., Balamurugan, A., Taus, E., Elliott, J., Krogstad, P., Tobin, N.H., Ferbas, K.G., Kitchen, S.G., Aldrovandi, G.M., Rimoin, A.W., Yang, O.O., 2021. Primary, recall, and decay kinetics of SARS-CoV-2 vaccine antibody responses. *ACS Nano* 15 (7), 11180–11191.
- Ioffe, S., Szegedy, C., 2015. Batch normalization: accelerating deep network training by reducing internal covariate shift. In: *International Conference on Machine Learning*. PMLR, pp. 448–456.
- Krahling, V., Halwe, S., Rohde, C., Becker, D., Berghofer, S., Dahlke, C., Eickmann, M., Ercanoglu, M.S., Gieselmann, L., Herwig, A., Kupke, A., Müller, H., Neubauer-Radel, P., Klein, F., Keller, C., Becker, S., 2021. Development and characterization of an indirect ELISA to detect SARS-CoV-2 spike protein-specific antibodies. *J. Immunol. Methods* 490, 112958.
- Lee, H., Dellatore, S.M., Miller, W.M., Messersmith, P.B., 2007. Mussel-inspired surface chemistry for multifunctional coatings. *Science* 318 (5849), 426–430.
- Liu, H., Dai, E., Xiao, R., Zhou, Z., Zhang, M., Bai, Z., Shao, Y., Qi, K., Tu, J., Wang, C., Wang, S., 2021a. Development of a SERS-based lateral flow immunoassay for rapid and ultra-sensitive detection of anti-SARS-CoV-2 IgM/IgG in clinical samples. *Sensor. Actuator. B Chem.* 329, 129196.
- Liu, Y., Ai, K., Liu, J., Deng, M., He, Y., Lu, L., 2013. Dopamine-melanin colloidal nanospheres: an efficient near-infrared photothermal therapeutic agent for in vivo cancer therapy. *Adv. Mater.* 25 (9), 1353–1359.
- Liu, Y., Zhan, L., Qin, Z., Sackrison, J., Bischof, J.C., 2021b. Ultrasensitive and highly specific lateral flow assays for point-of-care diagnosis. *ACS Nano* 15 (3), 3593–3611.
- Loshchilov, I., Hutter, F., 2017. Decoupled Weight Decay Regularization arXiv preprint arXiv:1711.05101.
- Lowe, D.G., 1999. Object recognition from local scale-invariant features. In: *Proceedings of the Seventh IEEE International Conference on Computer Vision*, pp. 1150–1157. Ieee.
- Lv, H., Wu, N.C., Tsang, O.T.-Y., Yuan, M., Perera, R.A.P.M., Leung, W.S., So, R.T.Y., Chan, J.M.C., Yip, G.K., Chik, T.S.H., Wang, Y., Choi, C.Y.C., Lin, Y., Ng, W.W., Zhao, J., Poon, L.L.M., Peiris, J.S.M., Wilson, I.A., Mok, C.K.P., 2020. Cross-reactive antibody response between SARS-CoV-2 and SARS-CoV infections. *Cell Rep.* 31 (9), 107725.
- Meredith, P., Sarna, T., 2006. The physical and chemical properties of eumelanin. *Pigm. Cell Res.* 19 (6), 572–594.

- Mohammad Lukman, Y., Nor Dyana, Z., Rahmah, N., Khairunisak, A.R., 2018. Development and evaluation of colloidal gold lateral flow immunoassays for detection of *Escherichia Coli*O157 and *Salmonella*Typhi. *J. Phys. Conf. Ser.* 1082, 12049.
- Mohit, E., Rostami, Z., Vahidi, H., 2021. A comparative review of immunoassays for COVID-19 detection. *Expet Rev. Clin. Immunol.* 17 (6), 573–599.
- Molnár, Á., 2020. Polydopamine – its prolific use as catalyst and support. *Material. ChemCatChem* 12 (10), 2649–2689.
- Muruato, A.E., Fontes-Garfias, C.R., Ren, P., Garcia-Blanco, M.A., Menachery, V.D., Xie, X., Shi, P.Y., 2020. A high-throughput neutralizing antibody assay for COVID-19 diagnosis and vaccine evaluation. *Nat. Commun.* 11 (1), 4059.
- Nel, A.E., Miller, J.F., 2021. Nano-enabled COVID-19 vaccines: meeting the challenges of durable antibody plus cellular immunity and immune escape. *ACS Nano* 15 (4), 5793–5818.
- Pastoriza-Santos, I., Pérez-Juste, J., Liz-Marzán, L.M., 2006. Silica-coating and hydrophobation of CTAB-stabilized gold nanorods. *Chem. Mater.* 18 (10), 2465–2467.
- Pritchard, E., Matthews, P.C., Stoesser, N., Eyre, D.W., Gethings, O., Vihta, K.-D., Jones, J., House, T., Vansteenhove, H., Bell, I., Bell, J.L., Newton, J.N., Farrar, J., Diamond, I., Rourke, E., Studley, R., Crook, D., Peto, T.E.A., Walker, A.S., Pouwels, K.B., 2021. Impact of vaccination on new SARS-CoV-2 infections in the United Kingdom. *Nat. Med.* 27 (8), 1370–1378.
- Roda, A., Cavallera, S., Di Nardo, F., Calabria, D., Rosati, S., Simoni, P., Colitti, B., Baggiani, C., Roda, M., Anfossi, L., 2021. Dual lateral flow optical/chemiluminescence immunosensors for the rapid detection of salivary and serum IgA in patients with COVID-19 disease. *Biosens. Bioelectron.* 172, 112765.
- Rublee, E., Rabaud, V., Konolige, K., Bradski, G., 2011. In: ORB: an Efficient Alternative to SIFT or SURF. 2011 International Conference on Computer Vision, pp. 2564–2571. Ieee.
- Shirshahi, V., Tabatabaei, S.N., Hatamie, S., Saber, R., 2020. Photothermal enhancement in sensitivity of lateral flow assays for detection of E-coli O157:H7. *Colloids Surf. B Biointerfaces* 186.
- Soh, J.H., Chan, H.M., Ying, J.Y., 2020. Strategies for developing sensitive and specific nanoparticle-based lateral flow assays as point-of-care diagnostic device. *Nano Today* 30.
- Tan, C.W., Chia, W.N., Qin, X., Liu, P., Chen, M.L., Tiu, C., Hu, Z., Chen, V.C., Young, B.E., Sia, W.R., Tan, Y.J., Foo, R., Yi, Y., Lye, D.C., Anderson, D.E., Wang, L.F., 2020. A SARS-CoV-2 surrogate virus neutralization test based on antibody-mediated blockage of ACE2-spike protein-protein interaction. *Nat. Biotechnol.* 38 (9), 1073–1078.
- Tani, H., Kimura, M., Tan, L., Yoshida, Y., Ozawa, T., Kishi, H., Fukushi, S., Saijo, M., Sano, K., Suzuki, T., Kawasuji, H., Ueno, A., Miyajima, Y., Fukui, Y., Sakamaki, I., Yamamoto, Y., Morinaga, Y., 2021. Evaluation of SARS-CoV-2 neutralizing antibodies using a vesicular stomatitis virus possessing SARS-CoV-2 spike protein. *Virology* 18 (1), 16.
- Wesemann, D.R., 2022. Omicron's message on vaccines: boosting begets breadth. *Cell* 185 (3), 411–413.
- Wu, Y., He, K., 2018. Group normalization. In: Proceedings of the European Conference on Computer Vision. ECCV, pp. 3–19.
- You, M., Lin, M., Gong, Y., Wang, S., Li, A., Ji, L., Zhao, H., Ling, K., Wen, T., Huang, Y., Gao, D., Ma, Q., Wang, T., Ma, A., Li, X., Xu, F., 2017. Household fluorescent lateral flow strip platform for sensitive and quantitative prognosis of heart failure using dual-color upconversion nanoparticles. *ACS Nano* 11 (6), 6261–6270.
- Zhao, J., Zhao, S., Ou, J., Zhang, J., Lan, W., Guan, W., Wu, X., Yan, Y., Zhao, W., Wu, J., Chodosh, J., Zhang, Q., 2020. COVID-19: coronavirus vaccine development updates. *Front. Immunol.* 11, 602256.
- Zheng, Z., Wang, P., Liu, W., Li, J., Ye, R., Ren, D., 2020. Distance-IoU loss: faster and better learning for bounding box regression. In: Proceedings of the AAAI Conference on Artificial Intelligence, pp. 12993–13000.
- Zhu, N., Zhang, D., Wang, W., Li, X., Yang, B., Song, J., Zhao, X., Huang, B., Shi, W., Lu, R., Niu, P., Zhan, F., Ma, X., Wang, D., Xu, W., Wu, G., Gao, G.F., Tan, W., 2020. A novel coronavirus from patients with pneumonia in China, 2019. *N. Engl. J. Med.* 382 (8), 727–733.